Title

Electrode-omics reveals epochs in silicon anode evolution underpinning electrochemomechanical resilience

Journal

Science Advances, 12(23)

ISSN

2375-2548

Authors

Ko, Youngmin

Kim, Dong-Min

Musgrove, Amanda L

et al.

Publication Date

2026-06-05

DOI

10.1126/sciadv.adx0930

ELECTROCHEMISTRY

Electrode-omics reveals epochs in silicon anode evolution underpinning electrochemomechanical resilience

Youngmin Ko[1,2]†, Dong-Min Kim[1]†, Amanda L. Musgrove[3], Hyungyeon Cha[4]‡, Liana Klivansky[1], Jaclyn Coyle[5], Andrew Dopilka[4], Stephen E. Trask[6], Marco-Tulio Fonseca Rodrigues[6], Young-Woon Byeon[7]§, Haegyeom Kim[7], Robert Kostecki[4], Gabriel M. Veith[3], Brett A. Helms[1,7]*

Here, we advance electrode-omics to identify evolutionary bursts by which ethereal locally superconcentrated electrolytes (LSCEs) mitigate silicon anode degradation through its epochs of electrochemical and chemical reactions. Anode composites form initially at high potential from ethereal solvent and anion [bis(fluorosulfonyl)imide (FSI^-)] redox. A first evolutionary burst at lower potential enriches composites with lithium alkoxides (LiO–R) and lithium oxide (Li_2O) and depletes sulfur oxides (SO_x) species. As the cells are cycled, a second evolutionary burst takes place, where previously extinct SO_x species reemerge concurrently with a loss of LiO–R and Li_2O. This identifies reactions rooted in "SuFEx" chemistry, where oxoanionic LiO–R and Li_2O species, electrochemically generated in the solid-electrolyte interphase, chemically react with FSI^- in the electrolyte to form emergent species. This sequence of evolutionary bursts produces a mechanically resilient composite that reduces silicon anode cracking over hundreds of cycles, leading to overpotential increase of only ~0.01 volts after 200 cycles.

INTRODUCTION

Silicon anodes are attractive for increasing the energy density of Li-ion batteries yet experience irreversible capacity loss when the electrode cracks across cycles of lithiation and delithiation (*1*–*5*). Whereas cracking of individual silicon particles has benefited from the installation of tailored solid-electrolyte interphases (SEI) (*6*–*9*), cracking within composite electrodes is more difficult to address, given the tendency of electrolytes to undergo decomposition at both conductive carbon additives and silicon active particles during formation and subsequent cycles of discharge and charge. Nano-sized silicon particles are relatively resistant to particle-level cracking compared to micrometer-sized particles; however, their degradation persists, driven by formation and evolution of SEI within the composite electrode matrix (*10*, *11*). Ideally, in situ formation of a passivating SEI at silicon is concomitant with the formation of a robust anode composite at minimal loss to the initial lithium inventory. This has been especially challenging to do in a silicon anode full cell that features cathodes, e.g., $LiFePO_4$ (LFP) and $LiNi_{0.8}Mn_{0.1}Co_{0.1}O_2$ (NMC811), as it requires additional attention to electrolyte oxidation to diverse compounds, many of which are corrosive to active materials and other cell components (*12*–*14*).

Here, we introduce an ethereal mixed-salt locally superconcentrated electrolyte (LSCE) containing lithium bis(fluorosulfonyl)imide (LiFSI) and lithium perchlorate ($LiClO_4$) that passivates high voltage cathodes yet unexpectedly also mitigates mechanical degradation of silicon anode, aiding capacity retention over hundreds of cycles (Fig. 1A). The benefits afforded were beyond what was achievable with an advanced carbonate electrolyte, whose cells produced anodes that were susceptible to cracking even after first lithiation. To understand this behavior, we conducted electrode-omics analyses (*12*, *15*, *16*) of the silicon composite anodes and found that in the presence of the mixed-salt LSCE, the chemical makeup changed in a sequence of evolutionary bursts. We found that composites initially formed, promoted by embedded carbon above 0.6 V (versus Li/Li^+) with the reduction of the ethereal solvent and FSI anion, leading to an enrichment of lithium alkoxides (LiO–R) and $LiSO_x$ chemical species. At lower potential (0.6 to 0.05 V), during the lithiation of silicon, we observed a first evolutionary burst consisting of accelerated solvent, $LiSO_x$, and perchlorate redox that enriched the anode composite with not only additional LiO-R but also Li_2O, concomitant with near-complete depletion of $LiSO_x$. After formation, a second evolutionary burst took place whereupon oxoanionic LiO–R and Li_2O species generated at top of charge subsequently reacted chemically with FSI anions in the electrolyte to regenerate previously extinct $LiSO_x$, $LiSO_x$NR, and R–OSO_x species. The reemergence of these species is firmly rooted in "SuFEx" chemistry (*17*, *18*) and contributes to long-lived silicon composite resilience. Together with its capability to passivate high voltage cathodes, the mixed-salt LSCE enabled the cycling of Si|NMC811 full cells with essentially no increase in average cell overpotential (~0.02 V), while that for the carbonate electrolyte control cells increased by 0.39 V. Likewise notable, the capacity retention of the mixed-salt LSCE cells was ~57% over 200 cycles, while that for the carbonate electrolyte control was only 4%. High-capacity pouch cells (40 mA·hour) operating under lean electrolyte operation (6.7 g $A{\cdot}hour^{-1}$) with the mixed-salt LSCE demonstrated a capacity retention of 66% after 100 cycles, showcasing the scalability of the electrolyte advance, while the carbonate reference led to the capacity retention of only 6% after the same cycling period.

[1]The Molecular Foundry, Lawrence Berkeley National Laboratory, Berkeley, CA 94720, USA. [2]Department of Chemistry, Sungkyunkwan University, Suwon 16419, Republic of Korea. [3]Chemical Sciences Division, Oak Ridge National Laboratory, Oak Ridge, TN 37831, USA. [4]Energy Storage and Distributed Resources Division, Lawrence Berkeley National Laboratory, Berkeley, CA 94720, USA. [5]Materials, Chemical, and Computational Science Center, National Laboratory of the Rockies, Golden, CO 80401, USA. [6]Chemical Sciences and Engineering Division, Argonne National Laboratory, Lemont, IL 60439, USA. [7]Materials Sciences Division, Lawrence Berkeley National Laboratory, Berkeley, CA 94720, USA.
*Corresponding author. Email: bahelms@lbl.gov
†These authors contributed equally to this work.
‡Present address: Ulsan Advanced Energy Technology R&D Center, Korea Institute of Energy Research, Ulsan 44776, Republic of Korea.
§Present address: Advanced Analysis and Data Center, Korea Institute of Science and Technology, Seoul 02792, Republic of Korea.

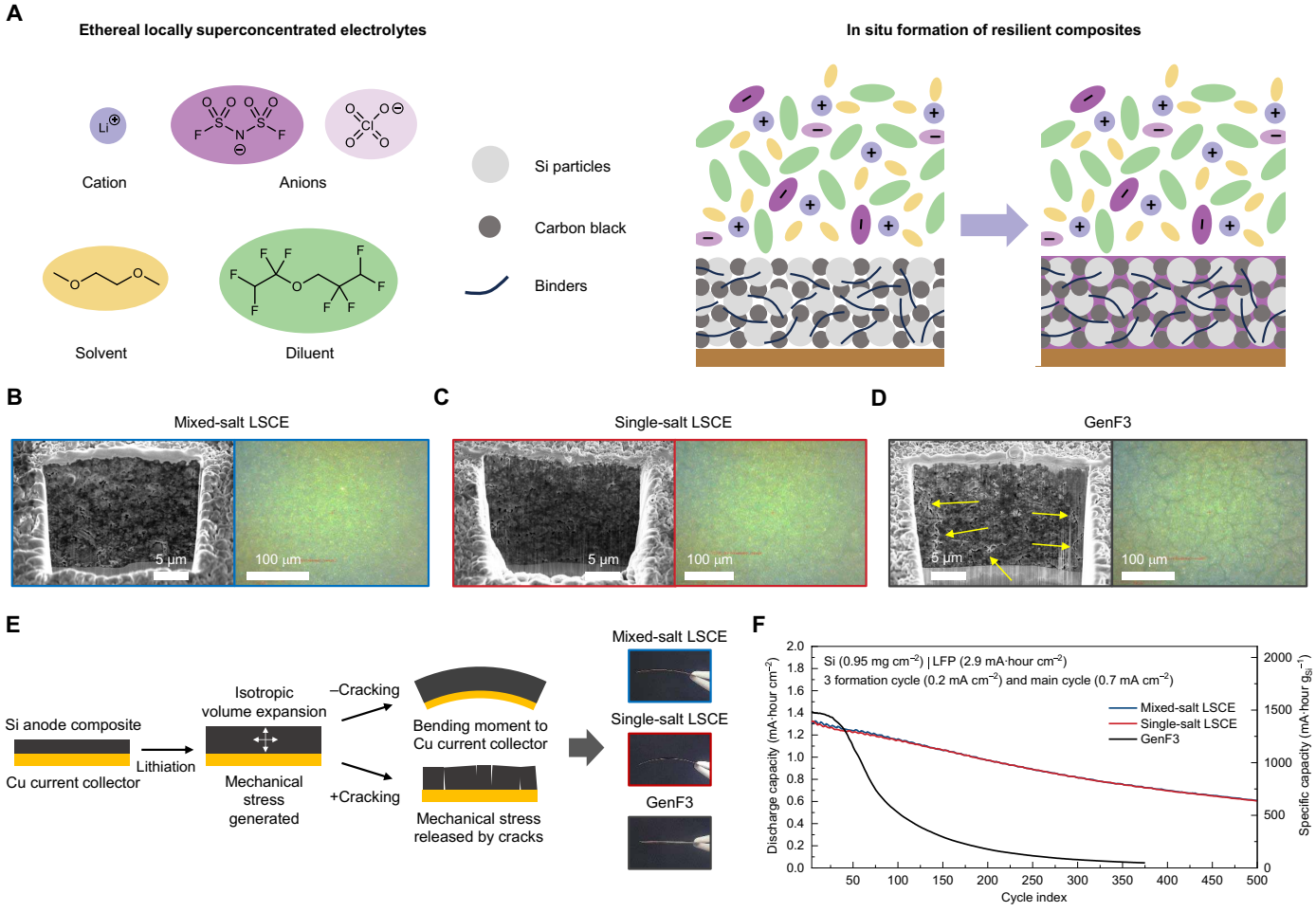

Fig. 1. In situ formation of resilient silicon anode composites by LSCEs to mitigate mechanical degradation. (**A**) Ethereal LSCEs create by their electrochemical reduction mechanically resilient silicon anode composites that resolve electrochemomechanical failure during volume expansion of silicon anode on lithiation. (**B** to **D**) Focused ion beam (FIB)–scanning electron microscopy (SEM) images, showing cross sections of lithiated silicon electrodes and surface images of silicon electrodes after 1 cycle (delithiated state) for cells assembled with either (B) mixed-salt ethereal LSCE, (C) single-salt ethereal LSCE, or (D) GenF3 carbonate electrolyte. Scale bars, 5 μm (FIB–SEM images, left) or 100 μm (optical images, right). (**E**) Bowing of silicon electrodes after lithiation and associated schematic showing isotropic volume expansion of silicon composites coated on copper current collectors and the respective impacts of composite resilience versus composite cracking on electrode bowing. (**F**) Capacity retention of Si|LFP cells assembled using a composite silicon anode (0.95 mg cm^{-2}) and an LFP cathode (~2.9 mA·hour cm^{-2}). Cells were cycled with a current density of 0.7 mA cm^{-2} after three formation cycles at 0.2 mA cm^{-2} using the voltage range of 2.6 to 3.4 V.

This sequence of evolutionary bursts and their subsequent epochs of relative stability are characteristic of a punctuated equilibrium by analogy to evolutionary biology, whereby changes to the genetic makeup, survival, or extinction of species occur abruptly rather than gradually over time. Furthermore, we offer electrode-omics as a framework for revealing important information regarding evolutionary events and epochs in the history of composite silicon anodes, permitting a reexamination and rescoping of how different electrolytes dictate important composite-level electrochemomechanical behaviors. This fossil record of the emergence, extinction, and evolution of chemical species in the cell should be taken into consideration alongside more well-understood particle-level phenomena for cell chemistries and architectures to emerge with practical designs. In this way, our work complements advances in silicon particle-size engineering (*19*–*21*), surface interphase tuning (*6*, *7*, *22*–*24*), particle encapsulation (*1*, *25*, *26*), and binder chemistry (*27*–*30*). Together, these pursuits are well positioned to make use of the lower materials overhead for lithium storage in silicon (0.23 Si atom per Li in $Li_{4.4}Si$) compared to graphite (6 C atoms per Li in LiC_6). In the future, identifying suitable combinations that ensure mechanical stability of silicon anodes will be essential and should consider the implications of the electrolyte chemistry from multiscale perspective, i.e., not only for particles but also the electrode wholistically as a composite, particularly when high areal capacity anodes are implemented to deliver high cell-level energy density commensurate with targets for electric vehicles and other use cases (*31*–*33*).

RESULTS

Electrolytes imparting mechanical resilience in silicon anodes

LSCEs are an emerging class of electrolytes where ions and solvents manifest primarily as clusters in a miscible yet nonsolvating matrix of diluent (*34*–*36*). They do not feature free solvent or dissociated

ions (fig. S1), which contributes to higher oxidative stability (fig. S2). Motivating our selection of an ethereal mixed-salt LSCE comprising LiFSI:$LiClO_4$:dimethoxyethane (DME):1,1,2,2-tetrafluoroethyl-2,2,3,3-tetrafluoropropyl ether (TTE) in a molar ratio of 0.9:0.1:2:2 was their ability to passivate high voltage cathodes (*12*). Less understood, however, was its complementarity with composite silicon anodes in Si|NMC811 cells. As controls, we also considered a single-salt LSCE featuring LiFSI:DME:TTE in a molar ratio of 1:2:2 and a single-salt carbonate electrolyte [GenF3; 1.2 M $LiPF_6$ in ethylene carbonate (EC)/ethyl methyl carbonate (EMC) with 3:7 wt:wt + 3 wt % fluoroethylene carbonate (FEC)]. The former control was selected to evaluate whether a mixed-salt LSCE affords unique advantages over a single-salt LSCE. The latter control was selected as a standard bearer for advanced carbonate electrolytes (*19*, *37*–*43*).

With these electrolytes in hand, we first observed how silicon electrodes behaved under volume change during lithiation and delithiation. We prepared composite silicon electrodes from ~200-nm silicon particles (80 wt %), a conductive carbon (Timcal C45; 10 wt %), and polyimide binder (P84; 10 wt %); the areal active material loading within the composite was 0.95 mg cm^{-2}. We lithiated the electrodes to ~1.9 mA·hour cm^{-2}, corresponding to a specific capacity of ~2000 mA·hour g_{Si}^{-1}, using a current density of 0.2 mA cm^{-2} (fig. S3). To visualize changes in composite electrode morphology after lithiation, we cross sectioned and imaged the electrodes by focused ion beam (FIB)–scanning electron microscopy (SEM) (Fig. 1, B to D). As expected, due to the volume expansion of silicon particles during lithiation, all electrodes showed an increase in thickness: specifically, final thickness of 13.2, 12.7, and 14.4 μm with mixed-salt LSCE, single-salt LSCE, and GenF3, respectively, compared to pristine silicon electrodes, whose average thickness was 9.5 μm (fig. S4). Electrodes lithiated with either of the two LSCEs showed dense cross sections without prominent mechanical degradation or cracking (Fig. 1, B and C). In stark contrast, electrodes undergoing formation with GenF3 showed signs of substantial mechanical degradation in their cross sections with numerous fracture events, extending from the top surface to the bulk of composite (Fig. 1D). This divergent mechanical behavior depending on electrolyte chemistry was further confirmed by nanoindentation using delithiated electrodes (*44*, *45*), where moduli for composite electrodes cycled with either of the LSCEs were higher than that for the electrode cycled with GenF3 (fig. S5). Optical images of the electrodes undergoing nanoindentation also showed evidenced severing cracking for the electrode cycled with the GenF3 electrolyte (Fig. 1, B to D). This absence of cracking in silicon anodes cycled with LSCEs also produced a persistent bowing effect for the retrieved lithiated electrodes (Fig. 1E). There was no bowing for mechanically compromised composite electrodes. We explain these outcomes as follows. In bilayers comprising the composite silicon electrode on a copper current collector, isotropic volume expansion of the composite without expansion of the copper induces a mechanical stress in response to the applied bending moment. Resilient composites should therefore show bowing; we observed bowing for the mixed-salt and single-salt LSCEs and no apparent structural abnormalities in the FIB-SEM images (Fig. 1, B and C). Composites that are less resilient, on the other hand, would not exhibit bowing because the mechanical stress would instead fracture the composite; we do not observe bowing in the case of the GenF3 carbonate electrolyte, which was concurrent with pervasive cracking throughout the silicon anode composite after lithiation (Fig. 1D).

To evaluate how electrolyte-dependent mechanical cracking influences silicon anode cycling stability, we assembled and tested Si|LFP cells using silicon electrodes (0.95 mg cm^{-2}) and LFP cathodes (2.9 mA·hour cm^{-2}), noting that LFP cathodes configured with excess capacity can sustain flat voltage profiles during cycling, inclusive of those driving electrolyte transformations. The cells were cycled with the current density of 0.2 mA cm^{-2} for three formation cycles and 0.7 mA cm^{-2} thereafter using a 2.6- to 3.4-V voltage window. Mixed-salt LSCE and single-salt LSCE resulted in cells whose galvanostatic cycling profiles and corresponding dQ/dV profiles evidenced low average cell overpotential increase over 200 cycles: 0.012 and 0.016 V, respectively (figs. S6 and S7). On the other hand, use of the GenF3 electrolyte resulted in cells whose average overpotential increased substantially over 200 cycles—by up to 0.136 V. As a result, Si|LFP cells cycled with either of the LSCEs achieved a capacity retention of ~74% after 200 cycles, while cells with GenF3 lost their capacity precipitously; only 10% was retained after 200 cycles (Fig. 1F).

After disassembling the cells, we found that composite silicon anodes cycled with LSCEs were mechanically resilient over at least 500 cycles, while those cycled with GenF3 were severely fractured (fig. S8). The high capacity retention for Si|LFP cells cycled with LSCEs is notable as the rate of increase in cell overpotential is low. The correlation between composite preservation and longer cycle life showcased an unexpected useful difference between LSCE and carbonate electrolytes and their readiness to manage the electrochemomechanics of composite silicon anodes. To support this understanding of silicon anode degradation at the composite level, we collected transmission electron microscopy images from silicon particles after 200 cycles (fig. S9). The micrographs showed that silicon particles experienced limited mechanical cracking during 200 times of cycling, attributed to the size of silicon particle and limited depth of lithiation less than 2000 mA·hour g_{Si}^{-1}. The absence of substantial particle cracking after 200 cycles indicated that the observed capacity retention profiles are tied to electrode-level phenomena, not to particle-level phenomena.

Evolutionary bursts and epochs in the evolution of the silicon anode

To better understand composite formation process and resulting resiliency afforded by LSCEs, we conducted cyclic voltammetry using Si|Li cells to observe a voltage-dependent electrolyte reduction behavior. We observed irreversible electrolyte reduction ranging 1.5 to 0.6 V (versus Li/Li^+), i.e., before lithiation of silicon. These reactions are promoted by the embedded carbon, as they are not observed in cells assembled with exclusively amorphous silicon active materials (fig. S10). We conducted x-ray photoelectron spectroscopy (XPS) to characterize the electrolyte reduction products at the different stages using silicon anodes retrieved at 0.60 V (electrolyte reduction promoted exclusively by carbon) and 0.05 V (electrolyte reduction promoted both by carbon and Si_xLi_y) during the first cathodic scan of cyclic voltammetry (figs. S11 to S15). Using XPS spectra, we obtained holistic chemical information of the various products by thorough apportionment of bonding classes (i.e., chemical species) for quantitative comparison across electrolytes and electrode potential (Fig. 2A and table S1).

Electrolyte reduction occurred in two distinct stages: Above 0.60 V (stage I), reactions are triggered proximally by the embedded carbon exclusively, while at 0.6 ~ 0.05 V (stage II), they are triggered both by carbon and at Si_xLi_y. Composites formed through stage I by

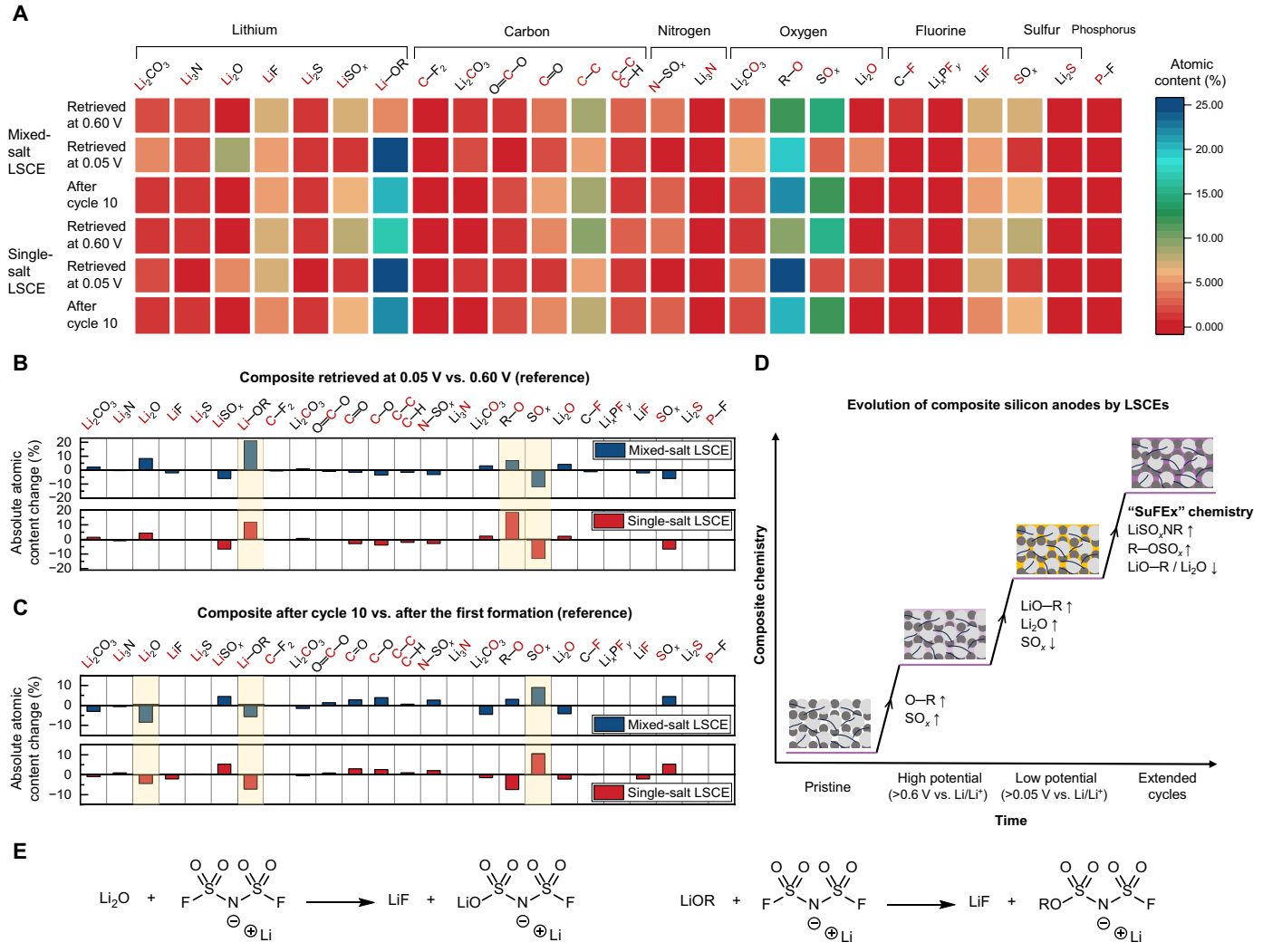

Fig. 2. Omics analyses of chemical species formed in situ from electrolyte decomposition in composite silicon anodes to elucidate composite formation process. (**A**) Apportionment of chemical species formed from the electrolyte within composite silicon anodes retrieved at 0.60 and 0.05 V during the first cathodic scan in cyclic voltammetry and after cycle 10, as analyzed by XPS. (**B**) Up- and down-regulation of the apportioned chemical species in composite silicon anodes retrieved at 0.05 V that feature both electrolyte reduction product at carbon and SEI@Si relative to those retrieved at 0.60 V that includes electrolyte reduction product at carbon as the reference (i.e., wild type). Notable columns are highlighted in yellow. (**C**) Up- and down-regulation of the apportioned chemical species in composite silicon anodes retrieved after cycle 10 relative to those retrieved after the first formation as the reference (i.e., wild type). Notable columns are highlighted in yellow. (**D**) Punctuated equilibrium view of composite electrode evolution, where the record of chemical species arising from electrochemical and chemical reactions is chronicled over formation and cycling, where we find evidence for evolutionary bursts and even extinction and reemergence events for specific species separated by epochs of (electro)chemical stability. (**E**) The re-emergence of previously extinct species is primarily tied to the chemistry of reactive oxoanions generated at top of charge, which react thereafter with endogenous LiFSI. These reactions are a previously unrecognized type of SuFEx chemistry.

LSCEs gave spectral signatures corresponding to primarily Li–OR, O–R, and SO_x species, indicating concurrent electrochemical FSI^- and DME reduction. However, composites that experienced both stage I and stage II evolved to feature chemistry with substantially less $LiSO_x/SO_x$ yet increases in Li–OR/O–R and Li_2O, which is largely distinct from those formed only after stage I. This evolutionary burst between two voltage ranges was analyzed by electrode-omics (*12*, *15*, *16*).

Specifically, omics enables quantitative assessment of all chemical species in the electrode composite. Up- or down-regulation of different species is reported relative to those for a reference (i.e., wild type). By reporting the up- or down-regulation of chemical species for composites retrieved at 0.05 V [electrolyte reduction promoted both by carbon and Si_xLi_y (stage I + stage II)] relative to those retrieved at 0.60 V [electrolyte reduction promoted exclusively by carbon (stage I)] as the reference (i.e., wild type), it becomes possible to understand voltage-dependent electrolyte reduction behavior (Fig. 2B). For example, composites retrieved at 0.60 V had 12 and 9% of their *O*-containing species tied to O–R for the mixed-salt and single-salt LSCE, respectively; composites subsequently retrieved at 0.05 V contained 19 and 28% of their *O*-containing species tied to O-R. Thus, the prevalence of O–R was up-regulated by up to 210%. In parallel, Li tied to Li–OR was up-regulated by 117% (from 12 to 26%) and 71% (from 17 to 29%) for the mixed-salt and single-salt

LSCEs, respectively. *O*-containing species tied to Li_2O were completely absent in composites at 0.60 V yet present at 8 and 4% for mixed-salt and single-salt LSCEs, respectively: The higher content of Li_2O in mixed-salt is from perchlorate redox. These informatics showcase how much higher the DME solvent activity is than that for FSI^- at Si_xLi_y during stage II (0.6 to 0.05 V). Concurrently, SO_x exhibited near-complete depletion with down-regulation by as much as 87% after experiencing stage II, confirming lower FSI^- activity than DME activity at Si_xLi_y. Notably, at top of charge after formation, highly reactive organic and inorganic oxoanionic species dominate with untold impacts.

Following this evolutionary burst, we cycled the cell and collected XPS spectra from composites after cycle 10 to understand the fate of the electrochemically generated LiOR and Li_2O. Here, our electrode-omics analysis sought to quantify the extent of up- or down-regulation of apportioned chemical species from composite after cycle 10 relative to those after the initial formation (i.e., retrieved at 0.05 V) as the wild-type reference (Fig. 2C, fig. S16, and table S1). We found that the succession of charge and discharge steps over this period resulted in a second evolutionary burst in composite chemistry (Fig. 2D). The most notable evolutionary change in the composites was the up-regulation of SO_x, tied to further reactions of FSI^-. Specifically, SO_x increased from 3 to 12% (+300%) in composites from the mixed-salt LSCE from cycle 1 to 10 and from 2 to 13% (+550%) in composites from the single-salt LSCE. In addition, *N*-containing species tied to N–SO_x were also up-regulated by up to +500%. Concurrent with the up-regulation of chemical species derived from FSI^-, we observed a down-regulation of highly reactive oxoanionic species. For example, Li–OR was down-regulated from 26 to 20% (−23%) and from 29 to 22% (−24%) in the mixed-salt and single-salt LSCEs, respectively. More notably, however, Li-containing species tied to Li_2O were found to be extinct.

We attribute the depletion and extinction of oxoanionic species concurrent with the enrichment of FSI^--derived species to SuFEx chemistry (*17*, *18*). Specifically, LiO-R and Li_2O appear to chemically react with FSI^- to form R–OSO_x and $LiSO_xNR$ species. These species are persistent during extended cycling, indicating that overreduction at exposed Li_xSi_y surfaces is minimal and electrical passivation of silicon particles has been achieved. To further support our claims of SuFEx chemistry within the SEI, we carried out ex situ chemical transformations by combining either LiFSI and LiOEt or LiFSI and Li_2O; to avoid any contributing influences of solvent, we conducted the transformations in the solid-state by ball milling. XPS analyses of the ball-milled products for both solid-state reactions showed an increase in Li—F bonding, while ball milling LiFSI alone did not induce a pronounced increase, indicating that SuFEx reactions occurred between LiFSI and both Li_2O and LiOEt (fig. S17). In addition, Fourier transform infrared spectroscopy on ball-milled mixtures exhibited attenuated ν(S—F) band (around 800 cm^{-1}) of LiFSI, shift, and broadening of $\nu_{as}(SO_2)$ mode from LiFSI and ν(C–O) mode from LiOEt (around 1380 and 1100 cm^{-1}), which is consistent with the proposed SuFEx reaction (fig. S18). The omics analysis further provides insight into the role of $LiClO_4$ in mixed-salt LSCE, which modifies the structure of ion clusters in a manner that increases the activity of FSI^- during SEI generation and consequently more pervasive SuFEx reactions. The reemergence of different sulfonyl species and the extinction of oxoanionic species (Fig. 2E) from chemical transformations during this second evolutionary burst is intriguing, particularly in the context of SuFEx chemistry. Moreover, the sequence of evolutionary bursts in the history of the cell, followed by periods of relative stability thereafter, is analogous to the concept of punctuated equilibrium in theories of evolution, where the population of species as a function of epoch (i.e., time) occurs in stepwise manner according to environmental cues and effects rather than continuously changing over time (Fig. 2D) (*46*).

Divergent evolution of silicon anodes with different electrolytes

We now expand our perspective beyond composite chemistry from LSCEs to understand the origin of mechanical resilience afforded by LSCEs in comparison to a highly optimized carbonate electrolyte, GenF3. As before, we collected XPS spectra from electrode composites formed with GenF3 after cycle 10 and compared them with those from LSCEs (Fig. 3A and fig. S15); for the electrode-omics analysis, we compared composite chemistries for different electrolytes in the same epoch (i.e., time). Up- or down-regulation of apportioned chemical species from LSCEs was visualized relative to those from GenF3 as wild-type reference (Fig. 3B). Aside from chemical species exclusive to either LSCEs or GenF3—such as N–SO_x or P–F, respectively—the most discernible difference in composite silicon anode composition is in the Li_2CO_3 content. Li_2CO_3 was down-regulated by ~90%: C species in the composite tied to Li_2CO_3 is 7% in cells cycled with GenF3; however, in cells cycled with the mixed-salt and single-salt LSCEs, C tied to Li_2CO_3 is less than 1%. Concurrently, we found that Li–OR were up-regulated up to ~9-fold in cells cycled with LSCEs: Li in the composite tied to Li–OR is only 2% when cycled with GenF3. By comparison, Li tied to Li-OR in cells cycled with mixed-salt or single-salt LSCEs is ~20%. The data also identify that bond cleavage is at C—O bonds in the carbonate solvents and not O—(C═O). Together, these data demonstrate that carbonate reduction is primarily responsible for the formation of composite silicon anodes in a dilute GenF3 electrolyte. Thus, fracture upon lithiation in the composite derived from GenF3 is dictated by the pervasiveness of rigid inorganic Li_2CO_3, which can be addressed by replacing carbonate electrolytes with ethereal LSCEs to create more resilient composites by depleting of Li_2CO_3 and enriched them with R–OSO_x, $LiSO_xNR$, and Li–OR species (Fig. 3C). We found minimal changes to the composite composition with mixed- versus single-salt LSCEs (Fig. 3D). Over the range of chemistries interrogated, changes in the absolute atomic content were no greater than 1.8%.

High-voltage stability and cathode-electrolyte interphase-omics

We next evaluated the electrolytes in NMC811 half-cells (NMC811 cathode with 14.2 mg cm^{-2}) to understand any implications of electrolyte composition on high voltage stability, an important requirement for Si|NMC811 cells to meet their energy density targets. Stable cycling of NMC811 cathodes requires a passivating self-terminating cathode-electrolyte interphase (CEI) that suppresses parasitic reactions and cathode corrosion at high voltage (*12*, *13*, *47*). To assess this, we measured the leakage current as a probe for CEI electrical passivation. After formation, undertaken over 3 cycles at a current density of 0.2 mA cm^{-2}, we then held the cell voltage at 4.25 V for 20 hours; we did the same after cycles 50 and 150 for cells cycled at a symmetric charge and discharge current density of 0.7 mA cm^{-2}. The mixed-salt LSCE completely suppressed leakage current evolution in a detectable current range over entire cycling (fig. S19),

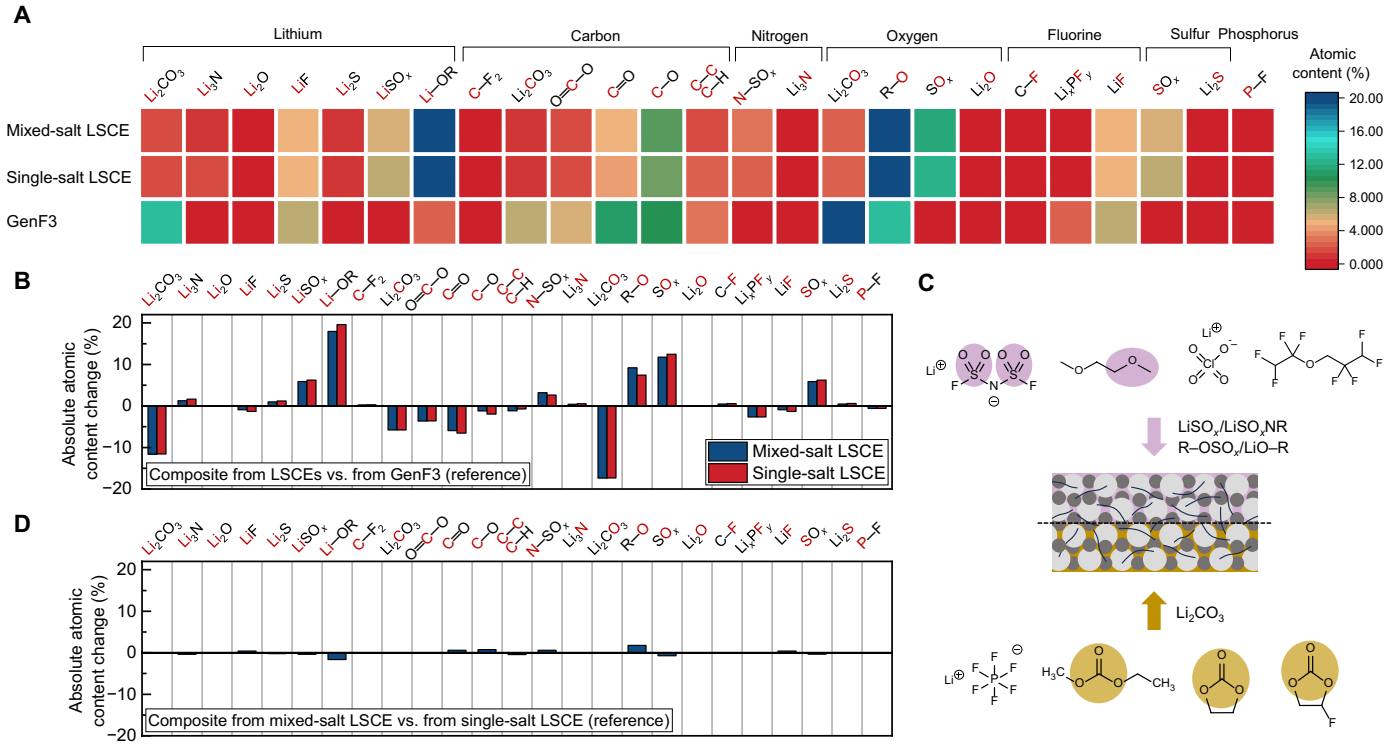

Fig. 3. Electrode-omics differentiates the chemistry in composite silicon anodes derived from ethereal and carbonate electrolytes. (**A**) Apportionment of chemical species within composite silicon anodes formed from LSCEs and GenF3 carbonate electrolyte analyzed by XPS. Silicon anodes were retrieved after 10 cycles. (**B**) Up- and down-regulation of the apportioned chemical species in composite silicon anodes from ethereal electrolytes relative to those from GenF3 carbonate electrolyte as the reference (wild type). (**C**) Identification of electrolyte components from LSCEs and GenF3 from which the chemical species formed in situ during cycling. The most prevalent chemical species were Li–OR and SO_x for LSCEs and Li_2CO_3 for GenF3. (**D**) Up- and down-regulation of the apportioned chemical species in composite silicon anodes from mixed-salt LSCE relative to single-salt LSCE as the reference (wild type).

which is notable, considering that the single-salt LSCE showed a substantial increase in leakage current by up to 260% over the same number of cycles. The carbonate-based GenF3 electrolyte is known to impart excellent electrochemical stability at this voltage when charging NMC811 cells, i.e., 4.25 V versus Li/Li^+. We found that the leakage current increased by 10% after cycle 150, from 21 to 23 μA cm^{-2}. The mixed-salt LSCE emerged as superior in its passivation of NMC811 during CEI generation.

We correlated salient differences in evolutionary trends in leakage current across the cycling history for the different electrolytes to CEI composition. To this end, we cycled NMC811 half-cells 100 times using the same protocol as that used to determine the leakage current and collected XPS spectra for the retrieved cathodes (fig. S20). We conducted omics as before by thorough apportionment of CEI chemical species by deconvoluting XPS spectra (fig. S21 and table S2). Up- and down-regulation of specific chemical species created by LSCEs can be discerned using GenF3 as the reference (fig. S22). Aside from chemical species exclusive to either LSCEs or GenF3—such as N–SO_x or P–F, respectively—we found that CEIs from LSCEs were substantially enriched in Li-F (from 0% in GenF3 to 5% in mixed-anion LSCE and 10% in single-anion LSCE) and exhibited down-regulations in several functionalities, such as Li–X (i.e., lithium compounds other than LiF) from 30% in GenF3 to 5 and 0.4% in the mixed-salt and single-salt LSCEs, respectively. It is evident that between ethereal LSCEs and carbonate electrolyte, GenF3 creates a CEI with distinct chemical properties as they do for silicon anodes. Unlike at the silicon anode, however, CEIs originating from mixed- and single-salt LSCEs are vastly different (fig. S23). Notably, the CEI created by the mixed-salt LSCE is up-regulated with functionalities such as CF_2 (+119%), C–C (+53%), and C–F (+36%) that are exclusive to TTE oxidation. Concurrently, down-regulation of functionalities exclusively derived from FSI^- oxidation was observed, such as LiF (−52%) and SO_x (−37%). This is consistent with our previous observation that the addition of ClO_4^- to LSCEs containing FSI^- alters the anodic reactivity of TTE and FSI^- to create a fluoroether-rich electrically passivating CEI (*12*). This CEI suppresses corrosive side reactions and minimizes the leakage current across NMC811 particle surfaces.

Electrode resilience and stability improves fitness in full cells

With this understanding of the benefits of the mixed-salt LSCE in Si|LFP and Li|NMC811 half-cells, we next evaluated the performance of Si|NMC811 full cells with them in place and by comparison to the single-salt LSCE and GenF3 electrolytes. We assembled Si|NMC811 full cells using silicon anodes (0.95 mg cm^{-2} and ~2.0 mA·hour cm^{-2}) and NMC811 cathodes (14.2 mg cm^{-2} and ~2.6 mA·hour cm^{-2}). These selections for electrode loadings considered that the first cycle Coulombic efficiency was ~70%, which informed a suitable N/P ratio (i.e., the ratio of electrode storage capacities for the negative and positive electrodes) that avoids prelithiation of the anode. We then formed Si|NMC811 full cells using current density of 0.2 mA cm^{-2} for 3 cycles over a voltage range of 3.2 to 4.2 V to form the

composite anode (inclusive of the anode SEI) and CEI on NMC811. We cycled them thereafter at a current density of 0.7 mA cm^{-2} over the same voltage range (Fig. 4, A to C, and fig. S24).

At the onset of cycling, Si|NMC811 cells exhibited similar initial areal capacity of ~1.6 mA·hour cm^{-2} for all electrolytes; however, the fade rate was differentiated by cycle 50. The cells assembled with the mixed-salt LSCE retained their capacity, while the cells with single-salt LSCE and GenF3 quickly lost reversible capacity after cycle 50 (Fig. 4, A to C). Cells with the mixed-salt LSCE led to average cell overpotential increase of only 0.02 V after cycle 200 (Fig. 4D). However, single-salt LSCE and GenF3 resulted in more than 10-fold larger increase in overpotential up to 0.26 and 0.39 V after the same cycling period, respectively. As a result, the Si|NMC811 cells with mixed-salt LSCE achieved capacity retention of 79.8% after cycle 100, while single-salt LSCE and GenF3 led to capacity retention of only 58.4 and 31.2% after cycle 100, respectively (Fig. 4E). Only the mixed-salt LSCE, which simultaneously mitigates electrode-level cracking of composite silicon anodes and sustainably low leakage current of NMC811 cathodes, enabled long-term cycling of Si|NMC811 full cells. On the other hand, single-salt LSCE and GenF3 each failed, either by not preserving electrode integrity of silicon anodes (GenF3) or by not adequately suppressing leakage current evolution on NMC811 cathodes (single-salt LSCE), resulting in accelerated overpotential increase and capacity fade rate.

To observe the cell degradation behavior, we retrieved electrodes and separators from Si|NMC811 full cells after cycle 200 (fig. S25).

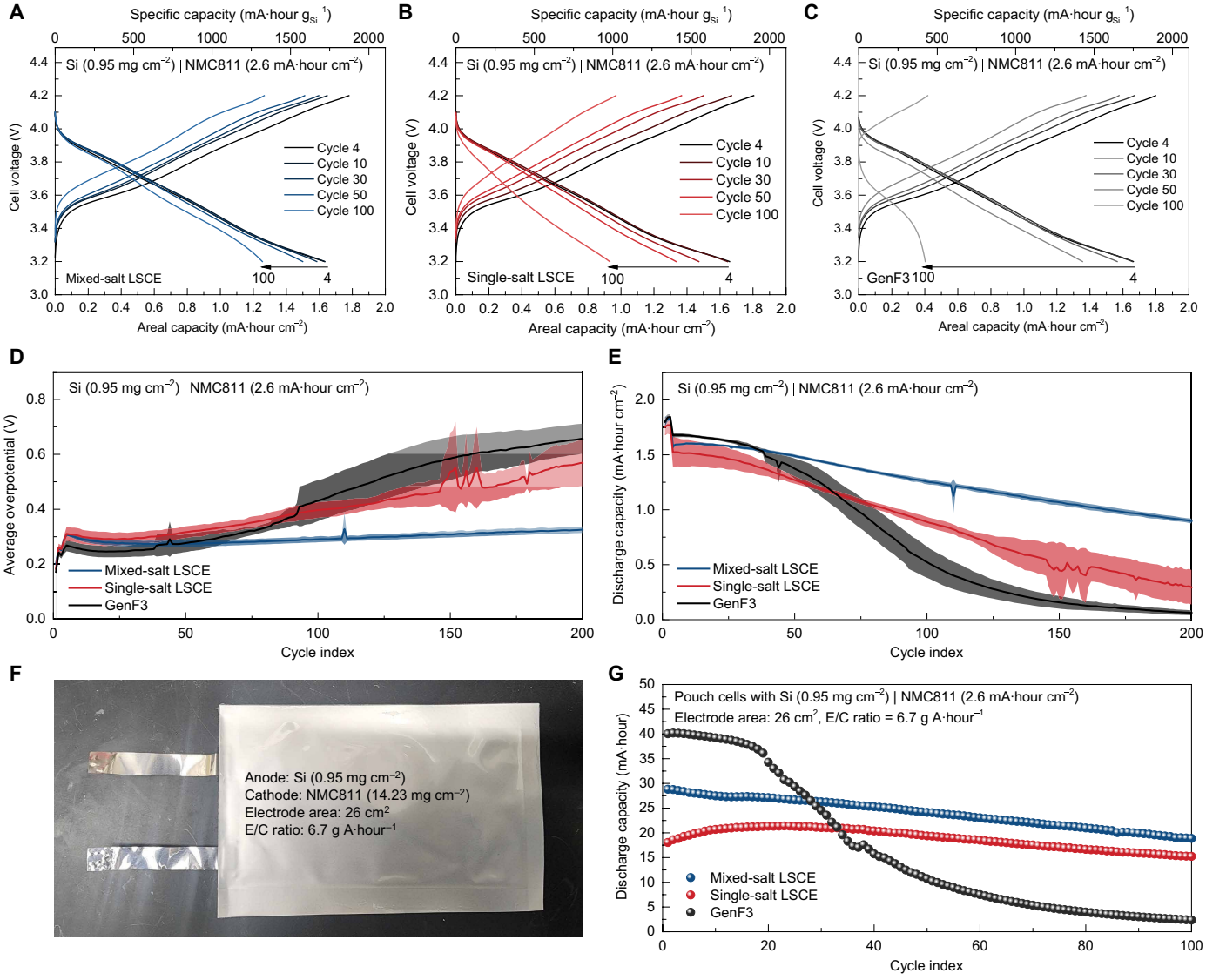

Fig. 4. Evaluation of Si|NMC811 full cells incorporating either of two LSCEs or GenF3. (**A** to **C**) Galvanostatic cycling profiles of Si|NMC811 cells cycled with (A) mixed-salt LSCE, (B) single-salt LSCE, and (C) GenF3. The cells were cycled with the current density of 0.7 mA cm^{-2} after three formation cycles at 0.2 mA cm^{-2} for the voltage range of 3.2 to 4.2 V. (**D** and **E**) (D) Average overpotential and (E) discharge capacity change during the cycling of Si|NMC811 full cells. The data were presented with the average and SD from three replicates. (**F**) The image of a Si|NMC811 pouch cell using electrodes with the same active loading level as coin cells and with the electrode area of 26 cm^2. Electrolyte weight–to–cathode capacity (E/C) ratio is 6.7 g A·$hour^{-1}$. (**G**) Discharge capacity change during the cycling of Si|NMC811 pouch cells with LSCEs and GenF3.

The silicon anode cycled with the mixed-salt LSCE did not show evident mechanical cracking or chemical residues on the separator. However, the cathode-facing surface of the separator retrieved from the cell cycled with single-salt LSCE was substantially contaminated by dark chemical residues tied to corrosive reactions on NMC811 cathodes. In addition, the silicon anode retrieved from the cells with GenF3 showed severe mechanical cracking, consistent with the observation from Si|LFP cells (fig. S8). The degradation behavior of cell components shows the importance of mitigating degradation of both electrodes to realize stable full cells and the importance of electrode-omics and failure analysis to reveal and understand the behaviors at the system level.

We further evaluated the electrolytes under practical conditions by assembling Si|NMC811 pouch cells. The same silicon anodes (0.95 mg cm^{-2}) and NMC811 cathodes (14.23 mg cm^{-2}) with the size of 26 cm^2 were used to assemble pouch cells, and electrolytes were injected to achieve the electrolyte weight–to–cathode capacity (E/C) ratio of 6.7 g A·$hour^{-1}$ (Fig. 4F). We then formed Si|NMC811 pouch cells using current density of 0.2 mA cm^{-2} for 3 cycles over a voltage range of 3.2 to 4.2 V. After formation, we degassed pouch cells and cycled them thereafter at a current density of 0.7 mA cm^{-2} over the same voltage range (Fig. 4G and fig. S26). The mixed-salt LSCE and single-salt LSCE achieved an initial capacity of 28.9 and 18.1 mA·hour , respectively, from Si|NMC811 pouch cells lower than GenF3 with an initial capacity of 40.2 mA·hour, which is attributed to lower ionic conductivity of LSCEs (*35*). Although LSCEs exhibited lower initial capacity than GenF3, they showed much slower capacity fade rate. The mixed-salt LSCE achieved capacity retention of 66% and reversible capacity of 19.1 mA·hour after cycle 100. The single-salt LSCE achieved reversible capacity of 15.4 mA·hour after cycle 100 lower than the mixed-salt LSCE due to low initial capacity. Unlike LSCEs, however, the pouch cells with GenF3 quickly lost reversible capacity, leading to capacity retention of only 6.3% and reversible capacity of 2.5 mA·hour after cycle 100. Performance trends across electrolytes were in line with the observation from Si|NMC811 coin cells, where the mixed-salt LSCE outperformed the other electrolytes. Coulombic efficiency of Si|NMC811 pouch cells with the mixed-salt LSCE around 99.5% further supports reversible electrode reactions achieved by the simultaneous mitigation of anode and cathode degradation (fig. S27). We note that the difference in initial capacity across electrolytes is primarily attributed to differences in ionic conductivity, which is more pronounced in pouch cells compared to coin cells, due to lower E/C ratio.

DISCUSSION

Understanding the origin of species associated with electrolyte and electrode degradation and prescribing on that basis mitigation strategies are paramount to battery technology development. Often, there are untapped opportunities to do so with electrolyte design, provided that there is a validated understanding of phenomena contributing to failure and its potential remedies. Electrode-omics provides key insights into structure, function, and evolution at molecular, composite, and cell levels. Correlating characteristics derived from omics analyses with the underlying electrical, chemical, and mechanical properties of the electrodes and cells provides the necessary context for diverse phenomena underpinning cell performance. In the present case study, a punctuated equilibrium emerges as theory to explain the history of electrode composite chemical species across evolutionary bursts and epochs, from electrochemical transformations within the composite and subsequent chemical reactions between species generated at interfaces that are in contact with the liquid electrolyte. A practical point of view supported by our work is that battery electrolytes should be designed not only for specific active materials in each electrode but also for the components therein, which are found to contribute immensely to the overall composition of the electrodes during formation and thereafter as the cell is cycled. Future work should more broadly consider targeted measures by which the electrolyte may be designed to suppress mechanical degradation of composite electrodes, not just electrical passivation of the active materials with ion-conducting materials.

MATERIALS AND METHODS

Materials

Lithium salts including LiFSI (Gotion), $LiClO_4$ (Sigma-Aldrich), and $LiPF_6$ (Strem Chemicals) were dried under vacuum at 60°C for at least 12 hours before use. Electrolyte solvents including DME (Gotion), TTE (SynQuest), EMC (Sigma-Aldrich), EC (Sigma-Aldrich), and FEC (Sigma-Aldrich) were dried with activated 4-Å molecular sieves before use. Electrolytes were prepared in Ar-filled glove box with $H_2O < 0.5$ parts per million (ppm) and $O_2 < 0.5$ ppm by dissolving lithium salt(s) in solvent(s). Silicon powder, LFP, and NMC811 powder were sourced from Oak Ridge National Laboratory, Johnson Matthey, and Targray, respectively. Silicon electrodes (0.95 mg cm^{-2}), LFP electrodes (20.5 mg cm^{-2}), and NMC811 electrodes (14.23 mg cm^{-2}) were supplied by the Cell Analysis, Modeling, and Prototyping (CAMP) facility at Argonne National Laboratory. Amorphous silicon film electrodes were fabricated using a one-half–inch–diameter (1.27 cm) fused silica wafer (University Wafer, U01-210714-1, Fused Silica JGS2). The quartz wafer was dc sputter coated (3 × 3″ TORUS Mag Keeper sputter guns) with Ti as an adhesion layer and Cu (1.0 μm) as the current collector on both sides. Amorphous silicon (50 nm) was sputtered onto one side from a silicon target (Kurt J. Lesker, Si, p-type, mono, 0.005 to 0.020 ohm·cm, 99.999% pure) at a power of 150 W for 8 min at a pressure of 1×10^{-4} mtorr under flowing argon. Celgard 2400 was used as a separator. Li metal foil (200 μm) was sourced from Honjo. CR2032 coin cell components were purchased from Hohsen. Aluminum laminate sheets (MediaTech, LLC) for pouch cells were cut, and two sides were sealed using a vacuum sealer and dried under vacuum alongside Celgard 2325 separator pillows before cell assembly. The separator pillows were prepared by fusing two sheets of Celgard 2325 together using a soldering tip at 450°C to trace a custom-made stencil. This was done to create a "pocket" in which the cathode can snugly fit inside to ensure proper alignment. Nickel and aluminum tabs were welded to the anode and cathode, respectively. The electrodes were then dried under vacuum at 80°C for at least 12 hours before being transferred to a glove box for assembly.

Characterization

XPS spectra were collected using a Thermo Fisher Scientific K-Alpha Plus instrument equipped with monochromatic Al Kα radiation (1486.7 eV) as the excitation source. Retrieved electrodes were gently washed with 200 μl of DME or EMC. Then, electrodes were transferred to XPS using air-free vacuum transfer module. Data

were collected and processed using the Thermo Fisher Scientific Avantage XPS software package. SEM/energy-dispersive x-ray analysis of Si anodes was conducted using EDAX Octane Super detector, installed to Helios G4 UX Dual Beam FIB-SEM (FEI/Thermo Fisher Scientific). An air-tight sample transfer module (Kammrath and Weiss Technologies) was used to prevent sample contamination. FIB milling was performed using a Ga ion beam on Helios G4 UX at Molecular Foundry in Lawrence Berkeley National Laboratory. Cross-sectional samples were prepared with an energy of 5 kV and a current density of 1.6 nA, applied at an incident angle of 52°C. For imaging, FIB-SEM images were acquired at an accelerating voltage of 20 kV and a monochromator working distance of 4 mm. A KLA iMicro Nanoindenter was used to conduct nanoindentation tests with a diamond Berkovich indenter tip: Twenty-five indents were taken on at least three locations on each electrode. Indentations were depth controlled to 5000 nm under a constant strain rate of 0.01 s^{-1} (in hertz). The Oliver–Pharr method was followed to determine the elastic modulus and hardness of the material at the target depth. Thermal drift during indentation remained below 0.1 nm s^{-1}.

Electrochemical experiments

Instrumentation

Cell assembly was conducted in an Ar-filled glove box with H_2O < 0.5 and O_2 < 0.5 ppm. Galavnostatic cycling of assembled cells was conducted using an Arbin LBT20084 potentiostat. All the cells were cycled in a temperature-controlled oven at 25°C.

Cell assembly

Si|LFP CR2032 coin cells were assembled using silicon electrodes (0.95 mg cm^{-2}, 15-mm diameter), polyethylene (PE) separators (19-mm diameter), and LFP cathodes (20.5 mg cm^{-2}, 14-mm diameter). Li|NMC811 CR2032 coin cells were assembled using Li metal foil (200 μm, 14-mm diameter), PE separators (19-mm diameter), and NMC811 cathodes (14.23 mg cm^{-2}, 12-mm diameter). Si|NMC811 CR2032 coin cells were assembled using silicon electrodes (0.95 mg cm^{-2}, 15-mm diameter), PE separators (19-mm diameter), and NMC811 cathodes (14.23 mg cm^{-2}, 14-mm diameter). Si anodes were assembled without prelithiation. All coin cells were assembled with 40 μl of electrolytes. For pouch cell assembly, Si anodes and NMC811 cathodes were punched to an area of 26.2 cm^2. The electrodes and separator were aligned inside the aluminum laminate sheets and vacuum sealed along the tabs. A total of 250 μl of electrolyte was transferred inside the pouch using a micropipette before creating a final seal under vacuum. The pouch cell was massaged to ensure complete wetting of the separator and electrodes before applying 10-psi pressure using custom-made stacking plates for electrochemical cycling.

Galvanostatic cycling

In advance of Si|LFP and Si|NMC811 CR2032 coin cells cycling, three formation cycles were carried out with the current density of 0.2 mA cm^{-2} for both discharging and charging using the cell voltage range of 2.6 to 3.4 V and 3.2 to 4.2 V, respectively. After formation, cells were cycling with the current density of 0.7 mA cm^{-2} with the same voltage range without constant voltage (CV) steps. For all pouch cells, three formation cycles were carried out with the current density of 0.2 mA cm^{-2} from 3.2 to 4.2 V. After the formation cycles were completed, the pouch cells were brought back into an inert glove box, cut open for degassing, and resealed under vacuum before subsequent cycling with the current density of 0.7 mA cm^{-2} from 3.2 to 4.2 V.

Cyclic voltammetry

Si|Li cells were assembled using two silicon sources of silicon anode composite and amorphous silicon film. Cell voltage was swept from the initial open circuit voltage (OCV) to 0.05 V and back to 1.5 V using a scan rate of 0.1 mV s^{-1}.

Leakage current tests

Leakage current of Li|NMC811 cells was measured by holding cell voltage at 4.25 V for 20 hours after formation, 50 cycles, and 150 cycles. Formation was carried out over 3 cycles with the current density of 0.2 mA cm^{-2} with voltage range of 3.0 to 4.25 V. After formation, the cells were cycled under the current density of 0.7 mA cm^{-2} for leakage current measurements.

Supplementary Materials

This PDF file includes:

Figs. S1 to S27
Tables S1 and S2

REFERENCES

1. M. Ko, S. Chae, J. Ma, N. Kim, H.-W. Lee, Y. Cui, J. Cho, Scalable synthesis of silicon-nanolayer-embedded graphite for high-energy lithium-ion batteries. *Nat. Energy* **1**, 16113 (2016).
2. S. Chae, M. Ko, K. Kim, K. Ahn, J. Cho, Confronting issues of the practical implementation of Si anode in high-energy lithium-ion batteries. *Joule* **1**, 47–60 (2017).
3. S. H. Choi, G. Nam, S. Chae, D. Kim, N. Kim, W. S. Kim, J. Ma, J. Sung, S. M. Han, M. Ko, H.-W. Lee, J. Cho, Robust pitch on silicon nanolayer–embedded graphite for suppressing undesirable volume expansion. *Adv. Energy Mater.* **9**, 1803121 (2019).
4. S. Chae, S. H. Choi, N. Kim, J. Sung, J. Cho, Integration of graphite and silicon anodes for the commercialization of high-energy lithium-ion batteries. *Angew. Chem. Int. Ed. Engl.* **59**, 110–135 (2020).
5. N. Kim, Y. Kim, J. Sung, J. Cho, Issues impeding the commercialization of laboratory innovations for energy-dense Si-containing lithium-ion batteries. *Nat. Energy* **8**, 921–933 (2023).
6. J. Chen, X. Fan, Q. Li, H. Yang, M. R. Khoshi, Y. Xu, S. Hwang, L. Chen, X. Ji, C. Yang, H. He, C. Wang, E. Garfunkel, D. Su, O. Borodin, C. Wang, Electrolyte design for LiF-rich solid–electrolyte interfaces to enable high-performance microsized alloy anodes for batteries. *Nat. Energy* **5**, 386–397 (2020).
7. Y. Ko, J. Bae, G. Chen, M. A. Baird, J. Yan, L. Klivansky, D.-M. Kim, S. E. Trask, M.-T. F. Rodrigues, G. M. Carroll, N. R. Neale, B. A. Helms, Topological considerations in electrolyte additives for passivating silicon anodes with hybrid solid–electrolyte interphases. *ACS Energy Lett.* **9**, 3448–3455 (2024).
8. Y.-F. Tian, S.-J. Tan, C. Yang, Y.-M. Zhao, D.-X. Xu, Z.-Y. Lu, G. Li, J.-Y. Li, X.-S. Zhang, C.-H. Zhang, J. Tang, Y. Zhao, F. Wang, R. Wen, Q. Xu, Y. G. Guo, Tailoring chemical composition of solid electrolyte interphase by selective dissolution for long-life micron-sized silicon anode. *Nat. Commun.* **14**, 7247 (2023).
9. H. Huo, M. Jiang, Y. Bai, S. Ahmed, K. Volz, H. Hartmann, A. Henss, C. V. Singh, D. Raabe, J. Janek, Chemo-mechanical failure mechanisms of the silicon anode in solid-state batteries. *Nat. Mater.* **23**, 543–551 (2024).
10. F. Wu, Y. Dong, Y. Su, C. Wei, T. Chen, W. Yan, S. Ma, L. Ma, B. Wang, L. Chen, Q. Huang, D. Cao, Y. Lu, M. Wang, L. Wang, G. Tan, J. Wang, N. Li, Benchmarking the effect of particle size on silicon anode materials for lithium-ion batteries. *Small* **19**, e2301301 (2023).
11. Z. Ma, T. Li, Y. L. Huang, J. Liu, Y. Zhou, D. Xue, Critical silicon-anode size for averting lithiation-induced mechanical failure of lithium-ion batteries. *RSC Adv.* **3**, 7398–7402 (2013).
12. Y. Ko, M. A. Baird, X. Peng, T. Ogunfunmi, Y.-W. Byeon, L. M. Klivansky, H. Kim, M. C. Scott, J. Chen, A. J. D'Angelo, J. Chen, S. Sripad, V. Viswanathan, B. A. Helms, Omics-enabled understanding of electric aircraft battery electrolytes. *Joule* **8**, 2393–2411 (2024).
13. W. Xue, M. Huang, Y. Li, Y. G. Zhu, R. Gao, X. Xiao, W. Zhang, S. Li, G. Xu, Y. Yu, P. Li, J. Lopez, D. Yu, Y. Dong, W. Fan, Z. Shi, R. Xiong, C. J. Sun, I. Hwang, W. K. Lee, Y. Shao-Horn, J. A. Johnson, J. Li, Ultra-high-voltage Ni-rich layered cathodes in practical Li metal batteries enabled by a sulfonamide-based electrolyte. *Nat. Energy* **6**, 495–505 (2021).
14. J. Cabana, B. J. Kwon, L. Hu, Mechanisms of degradation and strategies for the stabilization of cathode–electrolyte interfaces in Li-ion batteries. *Acc. Chem. Res.* **51**, 299–308 (2018).
15. N. Gehlenborg, S. I. O'donoghue, N. S. Baliga, A. Goesmann, M. A. Hibbs, H. Kitano, O. Kohlbacher, H. Neuweger, R. Schneider, D. Tenenbaum, A.-C. Gavin, Visualization of omics data for systems biology. *Nat. Methods* **7**, S56–S68 (2010).

16. K. J. Karczewski, M. P. Snyder, Integrative omics for health and disease. *Nat. Rev. Genet.* **19**, 299–310 (2018).
17. J. Dong, L. Krasnova, M. G. Finn, K. B. Sharpless, Sulfur (VI) fluoride exchange (SuFEx): Another good reaction for click chemistry. *Angew. Chem. Int. Ed. Engl.* **53**, 9430–9448 (2014).
18. A. S. Barrow, C. J. Smedley, Q. Zheng, S. Li, J. Dong, J. E. Moses, The growing applications of SuFEx click chemistry. *Chem. Soc. Rev.* **48**, 4731–4758 (2019).
19. M. C. Schulze, F. Urias, N. S. Dutta, Z. Huey, J. Coyle, G. Teeter, R. Doeren, B. J. T. de Villers, S.-D. Han, N. R. Neale, Control of nanoparticle dispersion, SEI composition, and electrode morphology enables long cycle life in high silicon content nanoparticle-based composite anodes for lithium-ion batteries. *J. Mater. Chem. A* **11**, 5257–5266 (2023).
20. J. Sung, N. Kim, J. Ma, J. H. Lee, S. H. Joo, T. Lee, S. Chae, M. Yoon, Y. Lee, J. Hwang, S. K. Kwak, J. Cho, Subnano-sized silicon anode via crystal growth inhibition mechanism and its application in a prototype battery pack. *Nat. Energy* **6**, 1164–1175 (2021).
21. P. Bärmann, M. Diehl, L. Göbel, M. Ruttert, S. Nowak, M. Winter, T. Placke, Impact of the silicon particle size on the pre-lithiation behavior of silicon/carbon composite materials for lithium ion batteries. *J. Power Sources* **464**, 228224 (2020).
22. Z. Cao, X. Zheng, Q. Qu, Y. Huang, H. Zheng, Electrolyte design enabling a high-safety and high-performance si anode with a tailored electrode–electrolyte interphase. *Adv. Mater.* **33**, e2103178 (2021).
23. H. Wu, G. Chan, J. W. Choi, I. Ryu, Y. Yao, M. T. McDowell, S. W. Lee, A. Jackson, Y. Yang, L. Hu, Y. Cui, Stable cycling of double-walled silicon nanotube battery anodes through solid–electrolyte interphase control. *Nat. Nanotechnol.* **7**, 310–315 (2012).
24. G. Yang, S. Frisco, R. Tao, N. Philip, T. H. Bennett, C. Stetson, J.-G. Zhang, S.-D. Han, G. Teeter, S. P. Harvey, Y. Zhang, G. M. Veith, J. Nanda, Robust solid/electrolyte interphase (SEI) formation on Si anodes using glyme-based electrolytes. *ACS Energy Lett.* **6**, 1684–1693 (2021).
25. D. Li, X. Huang, Q. Wang, Y. Yuan, Z. Yan, Z. Li, Y. Huang, X. Liu, Kinetics of methane production and hydrolysis in anaerobic digestion of corn stover. *Nat. Energy* **102**, 1–9 (2016).
26. N. Liu, Z. Lu, J. Zhao, M. T. McDowell, H.-W. Lee, W. Zhao, Y. Cui, A pomegranate-inspired nanoscale design for large-volume-change lithium battery anodes. *Nat. Nanotechnol.* **9**, 187–192 (2014).
27. S. Choi, T.-w. Kwon, A. Coskun, J. W. Choi, Highly elastic binders integrating polyrotaxanes for silicon microparticle anodes in lithium ion batteries. *Science* **357**, 279–283 (2017).
28. J. Ryu, S. Kim, J. Kim, S. Park, S. Lee, S. Yoo, J. Kim, N. S. Choi, J.-H. Ryu, S. Park, Room-temperature crosslinkable natural polymer binder for high-rate and stable silicon anodes. *Adv. Funct. Mater.* **30**, 1908433 (2020).
29. C. Wang, H. Wu, Z. Chen, M. T. McDowell, Y. Cui, Z. Bao, Self-healing chemistry enables the stable operation of silicon microparticle anodes for high-energy lithium-ion batteries. *Nat. Chem.* **5**, 1042–1048 (2013).
30. T.-w. Kwon, J. W. Choi, A. Coskun, The emerging era of supramolecular polymeric binders in silicon anodes. *Chem. Soc. Rev.* **47**, 2145–2164 (2018).
31. V. Viswanathan, A. H. Epstein, Y.-M. Chiang, E. Takeuchi, M. Bradley, J. Langford, M. Winter, The challenges and opportunities of battery-powered flight. *Nature* **601**, 519–525 (2022).
32. X. Zhang, Z. Ju, Y. Zhu, K. J. Takeuchi, E. S. Takeuchi, A. C. Marschilok, G. Yu, Multiscale understanding and architecture design of high energy/power lithium-ion battery electrodes. *Adv. Energy Mater.* **11**, 2000808 (2021).
33. H. S. Moon, W. Y. Park, T. Hendrickson, A. Phadke, N. Popovich, Exploring the cost and emissions impacts, feasibility and scalability of battery electric ships. *Nat. Energy* **10**, 41–54 (2025).
34. X. Cao, H. Jia, W. Xu, J.-G. Zhang, Review—Localized high-concentration electrolytes for lithium batteries. *J. Electrochem. Soc.* **168**, 010522 (2021).
35. M. A. Baird, J. Song, R. Tao, Y. Ko, B. A. Helms, Locally superconcentrated electrolytes for ultra-fast-charging lithium metal batteries with high-voltage cathodes. *ACS Energy Lett.* **7**, 3826–3834 (2022).
36. X. Ren, L. Zou, X. Cao, M. H. Engelhard, W. Liu, S. D. Burton, H. Lee, C. Niu, B. E. Matthews, Z. Zhu, C. Wang, B. W. Arey, J. Xiao, J. Liu, J.-G. Zhang, W. Xu, Enabling high-voltage lithium-metal batteries under practical conditions. *Joule* **3**, 1662–1676 (2019).
37. K. Schroder, J. Alvarado, T. A. Yersak, J. Li, N. Dudney, L. J. Webb, Y. S. Meng, K. J. Stevenson, The effect of fluoroethylene carbonate as an additive on the solid electrolyte interphase on silicon lithium-ion electrodes. *Chem. Mater.* **27**, 5531–5542 (2015).
38. N. M. Johnson, Z. Yang, M. Kim, D.-J. Yoo, Q. Liu, Z. Zhang, Enabling silicon anodes with novel isosorbide-based electrolytes. *ACS Energy Lett.* **7**, 897–905 (2022).
39. J. I. Preimesberger, F. L. E. Usseglio-Viretta, A. Verma, A. Singh, A. M. Colclasure, P. Walker, G. Teeter, G. F. Pach, J. Westgard, F. Urias-Cordero, N. R. Neale, J. E. Coyle, G. M. Carroll, The effect of nanoparticle size on calendar and cycle lifetimes of silicon anode lithium-ion batteries. *EES Batteries* **1**, 298–309 (2025).
40. P. R. Adhikari, G. F. Pach, J. Quinn, C. Wang, A. Singh, N. Prakash, A. Verma, A. Colclasure, G. A. Kliegle, G. M. Veith, N. R. Neale, G. M. Carroll, The origin of improved performance in boron-alloyed silicon nanoparticle-based anodes for lithium-ion batteries. *Adv. Energy Mater.* **15**, 2501074 (2025).
41. D. Salpekar, J. I. Premesberger, M.-T. F. Rodrigues, A. Singh, A. Verma, S. E. Trask, A. Colclasure, J. Coyle, A. N. Jansen, D. P. Abraham, W. Lu, High tensile alloy of copper to mitigate current collector deformation in silicon electrodes for lithium-ion batteries. *J. Power Sources* **655**, 237853 (2025).
42. A. L. Amanda, A. Verma, M.-T. F. Rodrigues, C. I. McBaniel, D. P. Abraham, S. Lam, A. Colclasure, A. Singh, B. L. Armstrong, G. M. Veith, Solid-state prealkylation of electrode architectures (SPEAR): Direct control of prelithiation levels in silicon anodes and electrochemical cycling. *Adv. Mater. Technol.* **11**, e02088 (2025).
43. Y. Ha, T. R. Martin, S. Frisco, L. Rynearson, M. C. Schulze, S.-D. Han, S. E. Trask, B. L. Lucht, G. Teeter, N. R. Neale, Evaluating the effect of electrolyte additive functionalities on NMC622/Si cell performance. *J. Electrochem. Soc.* **169**, 070515 (2022).
44. K. Hu, J. Zhang, X. Yu, J. Wang, X. Hu, Crack pinning enables stable cycling of micro-sized silicon anodes for wide-temperature lithium-ion batteries. *Energy Environ. Sci.* **18**, 7882–7893 (2025).
45. Z. Ma, D. Ruan, D. Wang, Z. Lu, Z. He, J. Guo, J. Fan, J. Jiang, Z. Wang, X. Luo, J. Ma, Z. Zhang, Y. You, S. Jiao, Selective methylation of cyclic ether towards highly elastic solid electrolyte interphase for silicon-based anodes. *Angew. Chem. Int. Ed.* **64**, e202414859 (2024).
46. S. J. Gould, N. Eldredge, Punctuated equilibrium comes of age. *Nature* **366**, 223–227 (1993).
47. S. Lee, L. Su, A. Mesnier, Z. Cui, A. Manthiram, Cracking vs. surface reactivity in high-nickel cathodes for lithium-ion batteries. *Joule* **7**, 2430–2444 (2023).

Acknowledgments

Funding: The information, work, or data here was funded by Silicon Anode Seedling Project from US Department of Energy's Vehicle Technologies Office. This research was supported, in part, by the US DOE's Vehicle Technologies Office under the Silicon Consortium Project, directed by B. Cunningham and managed by A. Burrell. X-ray photoelectron spectroscopy was conducted at the Molecular Foundry supported by the Office of Science, Office of Basic Energy Sciences of the US Department of Energy under contract no. DE-AC02-05CH11231, under user proposal MF-9583. Electrodes were produced by S. Trask and M. Rodrigues at the US DOE CAMP (Cell Analysis, Modeling, and Prototyping) Facility, Argonne National Laboratory. The CAMP Facility is fully supported by the DOE Vehicle Technologies Office. The views expressed in the article do not necessarily represent the views of the DOE or the US government. The US government retains and the publisher, by accepting the article for publication, acknowledges that the US government retains a nonexclusive, paid-up, irrevocable, worldwide license to publish or reproduce the published form of this work, or allow others to do so, for US government purposes. **Author contributions:** Conceptualization: Y.K., A.L.M., R.K., and B.A.H. Methodology: Y.K., D.-M.K., A.L.M., R.K., G.M.V., and B.A.H. Investigation: Y.K., D.-M.K., A.L.M., H.C., L.K., J.C., A.D., Y.-W.B., and G.M.V. Visualization: Y.K., D.-M.K., A.L.M., L.K., and B.A.H. Funding acquisition: R.K., G.M.V., and B.A.H. Project administration: R.K., G.M.V., and B.A.H. Supervision: H.K., R.K., G.M.V., and B.A.H. Writing—original draft: Y.K. and B.A.H. Writing—review and editing: Y.K., D.-M.K., A.L.M., L.K., J.C., A.D., M.-T.F.R., H.K., R.K., G.M.V., and B.A.H. Resources: D.-M.K., A.L.M., L.K., A.D., S.E.T., M.-T.F.R., and G.M.V. Validation: Y.K., D.-M.K., A.L.M., H.C., L.K., J.C., Y.-W.B., and G.M.V. Formal analysis: Y.K., D.-M.K., A.L.M., L.K., Y.-W.B., and R.K. Data curation: D.-M.K. **Competing interests:** B.A.H. has a financial interest in Sepion Technologies and Cyklos Materials. All other authors declare that they have no competing interests. **Data, code, and materials availability:** All data and code needed to evaluate and reproduce the results in the paper are present in the paper and/or the Supplementary Materials. Materials can be provided by the Lawrence Berkeley National Laboratory pending scientific review and a completed material transfer agreement. Requests for materials should be submitted to ipo@lbl.gov.

Submitted 28 February 2025
Accepted 23 April 2026
Published 5 June 2026
10.1126/sciadv.adx0930